Available online at www.sciencedirect.com

ScienceDirect

Journal of the European Ceramic Society 29 (2009) 1771–1779

www.elsevier.com/locate/jeurceramsoc

Influence of the deposition energy on the composition and thermal cycling behavior of $La_2(Zr_{0.7}Ce_{0.3})_2O_7$ coatings

Zhenhua Xu [a,b,c], Limin He [a,*], Rende Mu [a], Shimei He [a], Xinghua Zhong [b], Xueqiang Cao [b]

[a] *Beijing Institute of Aeronautical Materials, Department 5, P.O. Box 81-5, Beijing 100095, China*
[b] *State Key Laboratory of Rare Earth Resource Utilization, Changchun Institute of Applied Chemistry, Chinese Academy of Sciences, Changchun 130022, China*
[c] *Graduate School of Chinese Academy of Sciences, Beijing 100039, China*

Received 4 August 2008; received in revised form 9 October 2008; accepted 13 October 2008
Available online 22 November 2008

Abstract

Lanthanum–zirconium–cerium composite oxide ($La_2(Zr_{0.7}Ce_{0.3})_2O_7$, LZ7C3) coatings were prepared under different conditions by electron beam-physical vapor deposition (EB-PVD). The composition, crystal structure, surface and cross-sectional morphologies, cyclic oxidation behavior of these coatings were studied. Elemental analysis indicates that the coating composition has partially deviated from the stoichiometry of the ingot, and the existence of excess La_2O_3 is also observed. The optimized composition of LZ7C3 coatings could be effectively achieved by the addition of excess CeO_2 into the ingot or by properly controlling the deposition energy. Meanwhile, when the deposition energy is 1.15×10^4–1.30×10^4 J/cm^2, the coating has a similar X-ray diffraction (XRD) pattern to the ingot, and the thermal cycling life of the coating is also superior to other coatings. The spallation of the coatings occurs either within the ceramic layer approximately 6–10.5 μm above its thermally grown oxide (TGO) layer or at the interface between ceramic layer and bond coat.

Keywords: Thermal barrier coatings; Thermal properties; ZrO_2; CeO_2; Structural applications

1. Introduction

An increase of thermal efficiency in gas turbine is directly connected with a high gas inlet temperature and, therefore, leads to the increased thermal loads on the materials used for turbine components.[1,2] The application of the advanced nickel-based superalloy in turbine blade material aiming at elevating inlet temperature is becoming more and more difficult. In addition, the amount of air that can be used for cooling in high-performance engines is limited.[3] To meet these requirements, thermal barrier coatings (TBCs) have been applied in aircraft propulsion and land-based power generation systems to increase turbine inlet temperature and the thermal efficiency. Consequently, there is an enormous interest in the use of TBCs in aircraft engines. The state-of-the-art and conventional TBC system usually consists of a ceramic topcoat of YSZ, a metallic bond coat (BC, MCrAlYX, M = Ni/Co, X = Hf, Ta, Re, Si) and a Ni-based superalloy substrate.[4] Currently, TBCs are usually produced by either EB-PVD or atmospheric plasma spraying (APS).

Yttria-stabilized zirconia (YSZ), especially zirconia containing 8 wt% yttria (8YSZ) is currently used as the standard material of TBCs due to its low thermal conductivity (2.1 W m^{-1} K^{-1}), relatively high thermal expansion coefficient (11×10^{-6} K^{-1}) and chemical inertness in combustion atmospheres.[5] However, the major disadvantage of YSZ is the limited operation temperature of 1200 °C for the long-term application.[6] At higher temperatures, the t′-tetragonal phase transforms into the tetragonal and the cubic (t + c) phases. During cooling, the t-phase will further transform into the monoclinic (m) phase, giving rise to the volume increase and resulting in the formation of cracks in the coating.[7,8] Moreover, the sintering-induced volume shrinkages would degrade the columnar structure of EB-PVD coatings and raise the elasticity modulus and, as a result, restrict the favorable strain tolerance of the coating.[5] On the other hand, in the next generation of advanced engines, further increases in thrust-to-weight ratio will require even

---

[*] Corresponding author. Tel.: +86 10 62496456; fax: +86 10 62496456.
E-mail address: he_limin@yahoo.com (L. He).

0955-2219/$ – see front matter © 2008 Elsevier Ltd. All rights reserved.
doi:10.1016/j.jeurceramsoc.2008.10.005

higher gas temperature. This means that higher surface temperatures and larger thermal gradients are expected in advanced TBCs as compared to the conventional YSZ TBCs. In order to overcome these disadvantages of YSZ and meet the ambitious design goal, the search for new candidate materials with even lower thermal conductivity, higher operating temperature, better sintering resistance and phase stability at even higher temperature has been intensified in the last decade. Several ceramic materials such as Al_2O_3, TiO_2, mullite, $CaO/MgO + ZrO_2$, $CeO_2 + YSZ$, silicates, lanthanum aluminate, zircon, metal–glass composite, garnet ($Y_3Al_xFe_{5-x}O_{12}$) and zirconium phosphate ($(Ca/Mg)Zr_4–(PO_4)_6$) have been evaluated as TBCs materials.[9] The selection of TBCs materials is restricted by some basic requirements such as: (1) high melting point, (2) no phase transformation between room temperature and operation temperature, (3) low thermal conductivity, (4) chemical inertness, (5) thermal expansion match with the metallic substrate, (6) good adherence to the metallic substrate, and (7) low sintering rate of the porous microstructure.[8–10] Therefore, the number of materials that can be used as new TBCs is very limited. So far, although a few materials have been evaluated as the candidates for TBCs, no single material satisfies all requirements.

Among the interesting candidates for TBCs, the rare earth zirconates have been investigated and the results indicate that these materials are significant for the top ceramic materials for future TBCs. Especially those materials with pyrochlore structures and high melting points, lanthanum zirconate ($La_2Zr_2O_7$, LZ) shows promising thermo-physical properties and has attracted a great attention. LZ has a lower thermal conductivity ($1.56\,W\,m^{-1}\,K^{-1}$) than YSZ, a cubic pyrochlore structure which is stable up to its melting point (2300 °C), and it has been proposed as a promising TBCs material.[5,8,11–15] However, the relatively low thermal expansion coefficient of LZ leads to high thermal stress between the LZ coating and the metallic bond coat, and it also has a low fracture toughness. It is well known that, CeO_2 has high thermal expansion coefficient, which indicates that the thermal expansion coefficient of $La_2Zr_2O_7$ may be enhanced by CeO_2 doping.[16,17]

However, $La_2Zr_2O_7$ ceramic material doped by CeO_2 for TBCs has not been investigated in detail up to now, and no thermal cycling life result is available. Lanthanum–zirconium–cerium composite oxide ($La_2(Zr_{0.7}Ce_{0.3})_2O_7$, LZ7C3) as a candidate material for TBCs made by APS had previously reported by Cao.[3,16,18] On the other hand, EB-PVD coatings offer the potential for achieving higher engine operating temperatures and longer TBCs lifetimes due to its unique columnar microstructure.[19,20] EB-PVD has been recognized as an attractive method for fabricating TBCs for gas turbine hot section components. Hence it is necessary to investigate LZ7C3 TBCs prepared by EB-PVD. As previously reported in Refs. 19 and 21, during EB-PVD process, deposition energy has a significant effect on composition and performance of the coatings. Nevertheless, LZ7C3 TBCs prepared by EB-PVD under the different deposition energies have not been carried out up to now. The purpose of this study is to clarify the influence of the deposition energy on the composition and thermal cycling behavior of LZ7C3 coatings, and also study the failure behaviors of the coatings.

2. Experimental

2.1. Synthesis of LZ7C3

LZ7C3 powder with the desired composition was synthesized by solid-state reaction at 1400 °C for 12 h with La_2O_3 (99.99%, Chenghai Chemicals of Guangdong), CeO_2 (99.99%, Chenghai Chemicals of Guangdong) and ZrO_2 (99.5%, Chenghai Chemicals of Guangdong) as the starting materials. A deionized water-based suspension of LZ7C3 powder was ball-milled for 24 h with zirconia balls. The suspension was completely dried in a model with a diameter of 80 mm. After the cast-formation, the ingot was densified at 1500 °C for 12 h.

2.2. Preparation of bond coat and top ceramic coat

The directionally solidified Ni-based superalloy DZ125 (30 mm × 10 mm × 1.5 mm) was used as the substrate whose nominal composition was shown in Table 1. The substrates were sand-blasted for 15 min to remove the oxide layer before they were cleaned in ultrasonic bath. The substrates were fixed by the mechanical arm in the Arc Ion-plating (A-1000 Vacuum Arc Ion-Plating Unit, AIP) for the deposition of NiCrAlYSi bond coat (BC). The BC thickness was between 35 μm and 45 μm. The nominal composition of the BC was also listed in Table 1. After the deposition of BC, the substrates were heat-treated under high vacuum at 870 °C for 3 h. The top coating of LZ7C3 (90–110 μm in thickness) was fabricated by EB-PVD with mainly controlling the deposition energies, and these parameters for four LZ7C3 coating samples were listed in Table 2. The deposition energy used in this study was calculated in combination with current of electron beam, high-voltage, deposition time and e-beam focus. During the deposition, the substrate pre-heating power was set to be 8 kW, and the pattern of e-beam focus was basically kept constant on the surface of ingot. The averaged deposition pressure of EB-PVD working chamber was about 3×10^{-3} Pa and no oxygen was introduced into the vacuum chamber. The averaged substrate temperature for the depositions of LZ7C3 coating was 825 ± 25 °C. The substrate was rotated at a speed of 7 rpm.

Table 1
The nominal compositions (wt.%) of substrate DZ125 and bond coat.

Superalloy	Al	Cr	Co	Y	Si	Ta	Ti	W	Mo	Ni
Substrate (DZ125)	4.8–5.4	8.4–9.4	9.5–10.5	–	–	3.5–4.1	0.7–1.2	6.5–7.5	1.5–2.5	Balance
Bond coat (NiCrAlYSi)	6–10	20–25	–	0.08–0.4	0.4–0.8	–	–	–	–	Balance

Table 2
The LZ7C3 coating samples used in this study.

Sample	Deposition energy[a] ($\times 10^4$ J/cm^2)
A	1.45–1.60
B	1.30–1.45
C	1.15–1.30
D	1.0–1.15

[a] *Note*: Energy density (J/cm^2) used in this study is to express of deposition energy.

2.3. Oxidation and microstructure analysis

To evaluate the thermal shock resistance of the coatings, the cyclic oxidation test of samples A–D were heated in a furnace at 1100 °C for 30 min followed by removing out for cooling down with airflow for 5 min. The heating-up and then cooling-down makes one oxidation cycle, and this process was repeated until 5% area of the ceramic coat was delaminated, and the cycling number was then regarded as the thermal cycling life of TBCs. Meanwhile, after the cyclic oxidation for a certain time, the samples were also weighted with a balance, and the weight change as a function of oxidation time was recorded.

The coating samples were embedded in a transparent cold-setting epoxy and polished with diamond pastes down to 1 μm followed by etching with an acid solution of HCl and HNO_3 (volume ratio $HCl/HNO_3 = 3/1$). Scanning electron microscope (SEM, FEI-Quanta 600) equipped with EDS (Oxford INCAx-sight 6427) was applied for the microstructure and composition evaluation. X-ray diffraction (XRD, Rigaku D/Max 2500) with Cu Kα radiation at a scan rate of 4°/min was used for the phase determination of LZ7C3 ingot and coatings.

3. Results and discussion

3.1. Composition of the coating

Chemical compositions of LZ7C3 ingot and the as-deposited coatings for samples A–D are listed in Table 3. The ingot is basically stoichiometric $La_2(Zr_{0.7}Ce_{0.3})_2O_7$ by taking into account the experimental error. After deposition, the ratio of $La_2O_3/ZrO_2/CeO_2$ in the as-deposited coatings for samples A–D analyzed by EDS has deviated from the starting ingot. Obviously, as compared to the starting ingot, the content of La_2O_3 in the four coatings has increased, whereas the content of ZrO_2 has decreased. Differently, the content of CeO_2 has fluctuated in the range of 13.85–20.08 wt.%, and no visible trend is gained. The possible reasons for these phenomena are: (1) the surface temperature of the ingot is very high during the deposition, and different evaporation rates of the constituents might lead to the stoichiometry change when the material is heated; (2) the three constituents have different vapor pressures (8×10^{-5} atm, 9×10^{-7} atm and 2×10^{-2} atm at 2500 °C for La_2O_3, ZrO_2 and CeO_2, respectively[6,22]); (3) from the calculation of Madelung energy of the pyrochlore structure ($A_2B_2O_7$), ZrO_2 is thermally more stable than La_2O_3.[23] It can be seen from Tables 2 and 3, the higher is the deposition energy, the more is the content of La_2O_3 in the coating. It could further explain the faster evaporation of La_2O_3 than ZrO_2 during deposition. Additionally, the amount of CeO_2 loss during deposition is higher than that of La_2O_3 (or ZrO_2) due to its high vapor pressure. (4) It exists a correlation between the chamber pressure and composition change during deposition.[5,24] The change in vapor pressure during deposition probably turns out to affect heavily the chamber pressure leading to deviate of composition. (5) The melting and evaporation behavior of the source material, ingot density, deposition rate and efficiency, gun power, e-beam focus, dwell time, chamber pressure and vapor cloud geometry are predominant factors to control the coatings' composition during deposition.[18,22,25]

It can be seen from Table 3, however, only the sample C has a stoichiometric composition near to the starting ingot, samples A, B and D have deviated from the theoretical values to some extent. In order to optimize the composition of the LZ7C3 coating, the contents of La_2O_3 and CeO_2 are synchronously adjusted in the starting ingot, and the content of ZrO_2 is kept constant. Correspondingly, the deposition parameters adopted during deposition are the same with the sample C, implying that the deposition energy is in the range of 1.15×10^4–1.30×10^4 J/cm^2. Fig. 1 shows the change of La/Ce ratio in coating with La/Ce ratio in ingot. The La/Ce ratio increases with increasing La/Ce ratio in ingots under the same evaporating and depositing parameters. To a certain extent, the desired composition of ceramic coating can be achieved either by changing the ingot composition or by slightly modifying the deposition parameters.

$La_2Zr_2O_7$ (LZ, pyrochlore) and $La_2Ce_2O_7$ (LC, disordered fluorite) have different crystal structures. In the series of $La_2(Zr_{1-x}Ce_x)_2O_7$, LZ7C3 is a mixture of pyrochlore and fluorite.[16] The main phase in LZ7C3 is LZ with a small solubility of LC, and this phase keeps pyrochlore structure. The second phase is a solid solution of LC and LZ with fluorite structure. In order to further understand the crystal structure of LZ7C3, XRD patterns of LZ and LC are also displayed in Fig. 2. Fig. 2 shows the XRD patterns of LZ7C3 ingot and the four as-deposited LZ7C3 coatings with different deposition energies. It

Table 3
EDS analysis of chemical compositions of LZ7C3 ingot and coatings.

Sample	La_2O_3 (wt.%)	ZrO_2 (wt.%)	CeO_2 (wt.%)	Composition
Theoretical value	54.16	28.68	17.16	$La_2Zr_{1.4}Ce_{0.6}O_7$
Starting ingot	53.86	28.19	17.82	$La_{1.98}Zr_{1.37}Ce_{0.62}O_7$
A	67.12	16.97	15.91	$La_{2.67}Zr_{0.90}Ce_{0.60}O_7$
B	64.13	15.79	20.08	$La_{2.55}Zr_{0.84}Ce_{0.77}O_7$
C	56.55	27.36	16.09	$La_{2.10}Zr_{1.35}Ce_{0.57}O_7$
D	65.84	20.31	13.85	$La_{2.58}Zr_{1.05}Ce_{0.51}O_7$

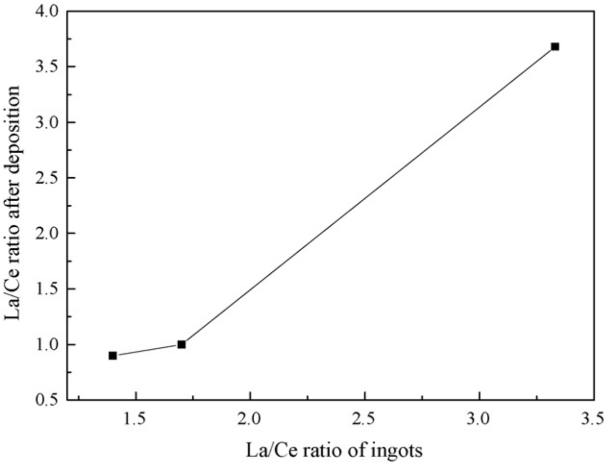

Fig. 1. La/Ce ratios before and after deposition.

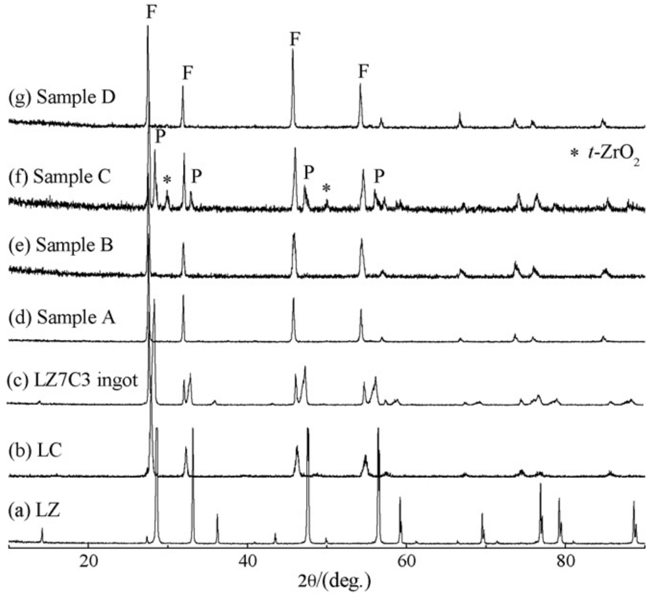

Fig. 2. XRD patterns of (a) LZ, (b) LC, (c) LZ7C3 ingot and (d)–(g) are four as-deposited LZ7C3 coatings, respectively. (*Note*: "F" and "P" represent "Fluorite" and "Pyrochlore" structures, respectively.)

can be seen from Fig. 2c and f, it is obvious that sample C has a similar XRD pattern with the ingot. The cubic pyrochlore and fluorite structures are the main phases even though two weak peaks of the *t*-ZrO_2 phase are also observed in the sample C. *t*-ZrO_2 phase is observed probably due to the partial decomposition of LZ7C3 during the overheating of EB-PVD, which is not detected in the samples A, B and D. These results are consistent with the elemental analysis as shown in Table 3. For the LZ7C3 ingot, the XRD peaks which belong to the pyrochlore structure are stronger than those of fluorite structure as shown in Fig. 2c. However, for the sample C, the situation is opposite. It indicates that a solid solution of LC and LZ with fluorite structure is more preferred formed in the LZ7C3 coating as compared to that of pyrochlore structure. Meanwhile, the preferred orientation growth of fluorite structure occurs in the $\langle 0\,0\,1 \rangle$ crystal direction. As previously reported in Refs.16 and 18, $La_2(Zr_{0.3}Ce_{0.7})_2O_7$ (LZ3C7) is composed of mainly fluorite with only a trace of pyrochlore. Interestingly, XRD patterns of samples A, B and D (Fig. 2d, e and g) are very similar to LZ3C7 and LC (Fig. 2b), only shift slightly the peaks to the smaller 2θ-value for samples A, B and D as compared with LC. Namely, it indicates that LZ3C7 coating might be prepared by LZ7C3 ingot under the deposition energy in the range of 1.30×10^4–1.60×10^4 J/cm^2. It is also interesting to see that all the peaks (Fig. 2d–g) slightly shift to the smaller 2θ-value (the larger *d*-values) compared with the ingot (Fig. 2c), because the formers have higher content of La_2O_3 than the latter. La^{3+} (0.106 nm) has a larger ionic radius than Zr^{4+} (0.079 nm) and Ce^{4+} (0.092 nm).

3.2. *Microstructure of the coating*

Fig. 3 shows the top surface and fractured cross-sectional SEM images of one of the representative as-deposited LZ7C3 coatings (sample C). As shown in Fig. 3a, the column tips show a cauliflower-like appearance, which is similar to the microstructure reported in Ref. 15. The surface morphology is basically similar to that of the YSZ coating which is previously reported in Ref. 26. Obviously, the gaps introduced due to the "shadowing effect" between column tips are also observed in Fig. 3a, which may partially release the concentration of thermal stress during long-term service. Namely, the tip edge of a columnar grain blocks the vapor flux and produces a shadow during rotation, which results in the formation of inter-columnar gaps.[27]

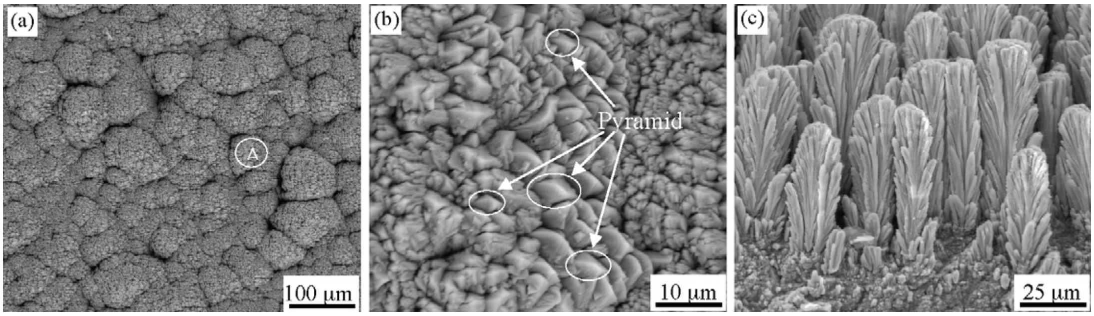

Fig. 3. SEM micrographs of the as-deposited LZ7C3 coating (sample C): (1) top surface with different magnifications: (a) 500×, (b) 5000×, the selected location A of (a); (2) (c) fractured cross-section.

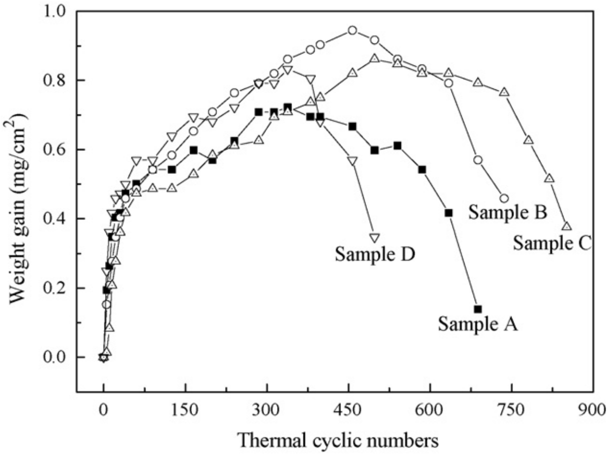

Fig. 4. Weight gains of samples A–D after thermal cycling test (1100 °C) for different periods of time.

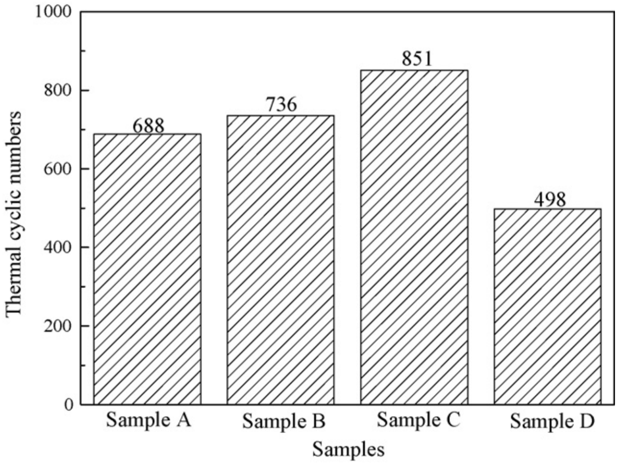

Fig. 5. The lifetimes of samples A–D after thermal cycling test.

From Fig. 3b, the column tips have a somewhat pyramidal shape, which refers to the cubic lattice of the pyrochlore (and/or fluorite) compound. The pyramidal diameters are measured to be approximately 2–4 μm. The fine pyramids appear to be connected with subset-prism, which may have displayed a different orientation than the main pyramid.

As shown in Fig. 3c, the feather-like microstructure within the columns normal to the bond coat surface is a representative morphology of the coating made by EB-PVD, and such a columnar structure has a very high tolerance to the thermal shock and is further helpful to the improvement of thermal cycling life.[6] It is found that each column consists of a number of subcolumns with different misorientations. Meanwhile, each column is irregularly distributed and the length of each featherarm is different from each other. On the other hand, without additional heating, the substrate temperature is determined by a combination of radiant heating from the melt, reflected electrons and vapor condensation.[19] Although the substrate temperature can be influenced to some extent owing to the different deposition energies used in this study, it is worth emphasizing that the averaged substrate temperature is basically kept at 825 ± 25 °C during deposition by properly adjusting the substrate pre-heating power.

3.3. Oxidation and thermal cycling behaviors of the coating

The weight changes of samples A–D during thermal cycling at 1100 °C are shown in Fig. 4. For samples A–D, their weights are gradually increased and then decreased due to the spallation of the top ceramic layer. After 338 cycles, the weight changes of samples A and D have unexpectedly decreased, which is different from samples B and C. However, the visible weight loss of samples B and C is balanced after 457 and 736 cycles, respectively. It is interesting to see from Fig. 4 that sample C has the lowest weight gain than that of the others before 338 cycles. The continuous weight loss of samples A–D after long-term exposure cycles is perhaps attributed to both edge chipping of the top ceramic coat and formation of non-adherent spinel phases at those parts of the sides of the specimens, where the bond coat surface is free of ceramic layer due to the TBCs processing. The weight increases of these coatings are in the order of B > D > A > C.

The lifetimes of samples A–D after thermal cycling test are shown in Fig. 5. Sample C has the longest lifetime of 851 cycles which corresponds to a total cycling time of 497 h. It has exceeded the criterion value of thermal cycling test in the field. In other words, it is not necessary to use an 8YSZ interlayer in this investigation. The results of thermal cycling test and EDS analysis (Figs. 4 and 5, and Table 3) indicate that: (1) the lower is the weight gain, the longer is the lifetime (sample C); (2) the earlier is the spallation of ceramic layer during cooling, the shorter is the lifetime (sample D); (3) the higher is the ZrO_2 content, the longer is the lifetime (sample C); (4) the lower is the CeO_2 content, the shorter is the lifetime (sample D); (5) although the lifetimes of samples A and B do not have remarkable differences, the excess content of La_2O_3 is likely to result in the premature failure of sample A compared with sample B. The possible reason is that it would absorb moisture from the air with the formation of $La(OH)_3$, leading to the swelling and then spalling of the coating. Therefore, the excess La_2O_3 in the coating is dangerous to the coating.

Fig. 6 shows the SEM images of LZ7C3 coatings' surface after spallation and corresponding EDS analyses. The gaps between column tips are closer and the micro-cracks originated on the surface of ceramic layer are correspondingly more for samples A and D than that of samples B and C. The possible reason is that the top ceramic layer is subjected to a tensile stress during heating. Micro-cracks between columnar grains could be easily induced because micro-cracks are able to release stresses in the top ceramic layer. It is expected that those micro-cracks would be beneficial in extending the thermal cycling lifetime of TBCs when they do not grow on a large-scale,[28] and this can explain the longer lifetimes of samples B and C than those of samples A and D. After thermal cycling, it can be seen from Fig. 6a and d that the grain boundaries between columnar grains become unclear, and the densification phenomenon is also observed. It is considering that the excess of La_2O_3 contained in the samples A and D due to the unreasonable deposition ener-

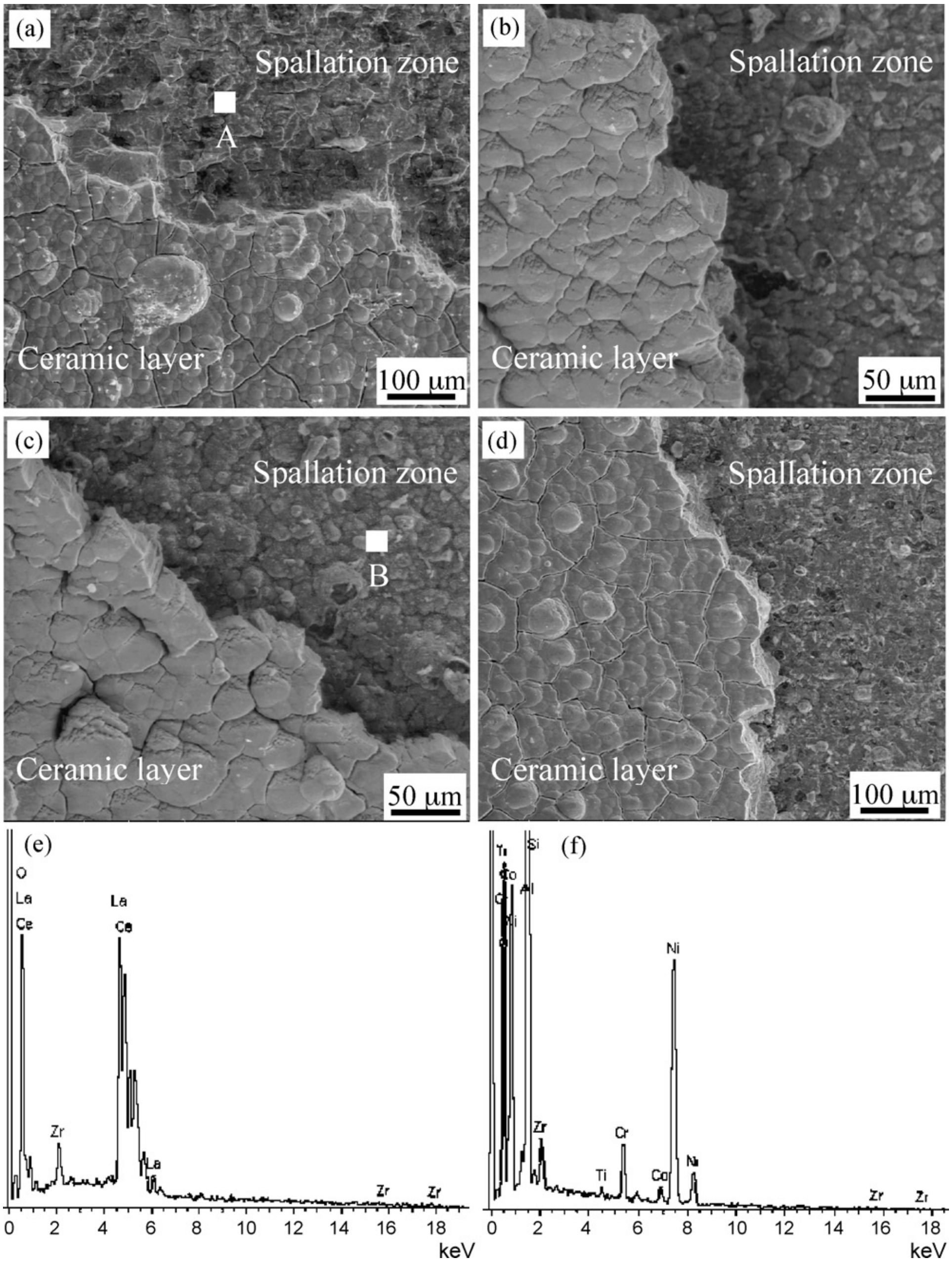

Fig. 6. SEM surface morphologies of the LZ7C3 coatings after spallation during thermal cycling test: (a)–(d) represent samples A–D, respectively. (e) and (f) are EDS spectra of area "A" in sample A and area "B" in sample C, respectively.

gies adopted is likely to influence the sintering-resistance ability of the coatings. The densified coatings can also reduce thermal stress/strain tolerance, which will have significant adverse effects on the durability of the TBCs.[29] On the other hand, as shown in Figs. 6a–d, the column tips are still cauliflower-like microstructure after spallation failure, indicating that LZ7C3 has a good thermal cycling behavior and low sintering ability. It has been proved that the LZ7C3 coating prepared by plasma-spraying has a very good sintering-resistance.[16,18] The EDS result presented in Fig. 6e indicates that the elements of La, Ce, Zr and O still exist on the surface of the spallation zone, it means that the spallation of the top ceramic layer (sample A) is likely to occur a little bit above the interface between ceramic layer and bond coat. The analogical EDS results for samples B–D are carried out, and one representative result is presented in Fig. 6f. The relative contents of Al, Ni and O are high, but contents of other elements such as Cr, Co, Zr, Ti or Si are low, implying that the spallation of the top ceramic layer is probably to occur at the interface between ceramic layer and bond coat. The possible failure mechanism of samples B–D is that a brittle Ni(Cr, Al)$_2$O$_4$ spinel phase developed during thermal cycling leads to the spallation of the coatings.

The cross-sectional SEM images of the LZ7C3 coatings before and after thermal cycling test are compared in Fig. 7. The cross-sectional SEM images of the as-deposited samples A–D are basically identical, and one of them is displayed in

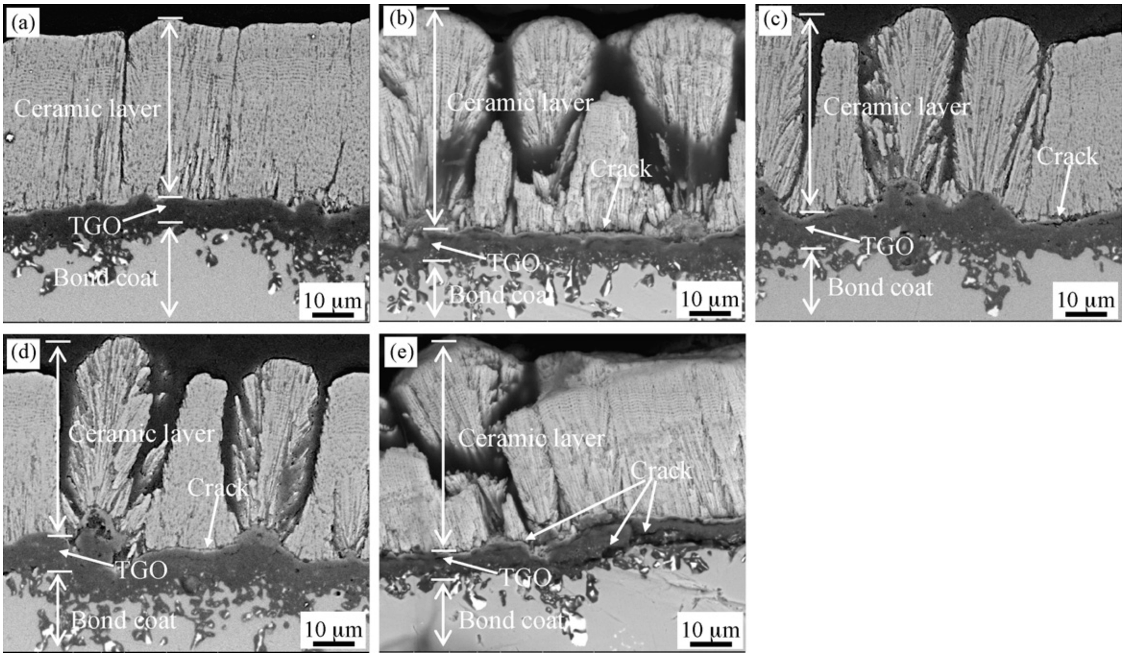

Fig. 7. Cross-sectional SEM (backscattered electron) images of the LZ7C3 coatings: (a) sample A before thermal cycling; (b)–(e) represent samples A–D after thermal cycling, respectively.

Fig. 7a. After thermal cycling, a black thin layer (∼6 μm in thickness) between the LZ7C3 coating and BC is clearly observed in Fig. 7b–e, and this thin layer is described as the thermally grown oxide (TGO) layer, implying that bond coat (BC) oxidation is still an important factor for coating failure. The TGO layer consists of mainly Al_2O_3 and some oxides of Cr, Co and Ni as proved by EDS, which data is not shown in this paper. As shown in Fig. 7a, the TGO layer with a thickness of ∼3.5 μm is also clearly observed in the coating before thermal cycling, and this thin layer is a result of the pre-oxidation of BC before deposition. The pre-oxidation can effectively prevent BC from the further oxidation during thermal cycling, leading to an increase of thermal cycling life of TBCs.[4] The internal-oxidation of BC for samples B and C seems to be more serious than that of samples A and D, it is possible attributed to the larger gaps existed interior of ceramic layer of the formers as compared to the latters. It seems that this phenomenon is consistent with the results shown in Fig. 4. The internal-oxidation of BC usually occurs by both the oxygen penetration through the inter-columnar gaps in the ceramic layer and oxygen-diffusion through the crystal lattice of the coating material.[30]

It can be carefully seen from Fig. 7b to d that a thin layer with a thickness of 0.7–1.2 μm is observed on the surface of TGO layer. Some cracks and pores below this layer are simultaneously appeared. Interestingly, it is found that the thicker is this layer, the shorter is the lifetime of the coatings. It is considering that the spinel phase of $Ni(Cr, Al)_2O_4$ could be largely accumulated into this layer, which is very brittle and harmful to low the interface bonding. On the other hand, at high temperature, the $LaAlO_3$ might be formed inside of this layer due to the chemical reaction between excess La_2O_3 and the as-formed Al_2O_3 at the interface between ceramic layer and TGO layer. $LaAlO_3$ has perovskite structure for temperature above 450 °C and it undergoes a phase transformation to a rhombohedral symmetry as the temperature is decreased, which results to structure inhomogeneity.[31,32] This could influence the thermal cycling lifetime of the LZ7C3 coatings. However, the exact mechanism behind is still unclear. In order to study the stability of LZ7C3 coating when it contacts TGO, a mixture of sample C and Al_2O_3 powders in a molar ratio of 50:50 was heated at 1100 °C for 48 h, and the XRD results are shown in Fig. 8. Obviously, the peaks belonging to $LaAlO_3$ are detected in Fig. 8, which further proves that LZ7C3 coating could react with the as-formed TGO layer during thermal cycling. Additionally, some transverse cracks are

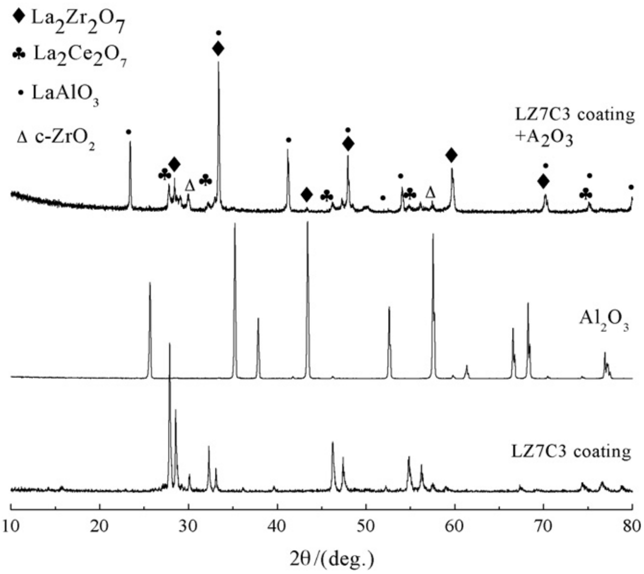

Fig. 8. XRD patterns of the mixture of LZ7C3 coating (sample C) and Al_2O_3 after being heated at 1100 °C for 48 h.

observed at the interface between the top ceramic layer and TGO layer for all samples after thermal cycling. Whereas the crack existed in sample C is not visible as compared to the others. This phenomenon may be regarded as one of factors to prolong the thermal cycling lifetime of sample C. As expected, the quality of sample C after thermal cycling test is better than other three samples, and the top ceramic layer is still adhered to the BC. For sample D, several cracks are produced inside of TGO layer and even prolonged down to the interface between TGO layer and BC surface. The acceleration of TGO degradation will have a significant impact on the durability of the TBCs, and further lead to TBCs delamination, resulting in the early failure of sample D. From Fig. 7b, the spallation zone is appeared in sample A within the ceramic approximately 6–10.5 μm above its TGO layer during cooling, consequently, this phenomenon is in accord with the EDS analysis presented in Fig. 6e. On the other hand, the mismatch in coefficient of thermal expansion between the top ceramic layer and BC results in residual stresses that can cause coatings' failure for samples A–D. In addition, during cooling of the thermal cycling process, a compressive stress is introduced, which tends to separate the LZ7C3 coatings from BC and finally causes the failure of TBCs. As shown in Fig. 7b–e, the LZ7C3 coatings still keep feather-like microstructure even after long-term thermal cycling, this phenomenon further confirms that the LZ7C3 coating has a good sintering-resistance.

4. Conclusions

LZ7C3 TBCs were prepared by EB-PVD under the different deposition energies, and the thermal cycling behaviors of the four coatings were also systematically studied. From our experimental investigation, the following conclusions can be obtained:

(1) The ratio of $La_2O_3/ZrO_2/CeO_2$ in the as-deposited LZ7C3 coatings has partially deviated from the starting ingot. The excess of La_2O_3 is contained in all the four coatings, indicating that LZ7C3 is decomposed during deposition. The optimized composition of LZ7C3 coatings could be effectively achieved by changing the ingot composition or by properly controlling the deposition energy.

(2) The main phases of the sample prepared under the deposition energy of 1.15×10^4–1.30×10^4 J/cm^2 has a similar XRD pattern to the ingot. However, other three samples have a very similar XRD pattern with LZ3C7 and LC. The sample deposited with a deposition energy of 1.15×10^4–1.30×10^4 J/cm^2 has the most optimal stoichiometric composition close to the ingot, and the best oxidation resistance performance and the longest thermal cycling life are among these coatings.

(3) The spallation of the top ceramic layer of the sample prepared under the deposition energy of 1.45×10^4–1.60×10^4 J/cm^2 may occur within the ceramic approximately 6–10.5 μm above its TGO layer, and the spallation locations of the other three samples are observed at the interface between ceramic layer and bond coat.

Acknowledgements

This work was financially supported by the projects of 2006241, NSFC-50825204 and A1320061002.

References

1. Mévrel, R., State of the art on high-temperature corrosion-resistant coatings. *Mater. Sci. Eng. A*, 1989, **120**, 13–24.
2. Cremer, R., Witthaut, M., Reichert, K., Schierling, M. and Neuschuetz, D., Thermal stability of Al–O–N PVD diffusion barriers. *Surf. Coat. Technol.*, 1998, **108/109**, 48–58.
3. Cao, X. Q., Application of rare earths in thermal barrier coating materials. *J. Mater. Sci. Thchnol.*, 2007, **23**, 15–35.
4. He, L. M., Effects of EB-PVD process TGO formation and growth within thermal barrier coatings. *Mater. Sci. Forum.*, 2007, **546–549**, 1781–1788.
5. Saruhan, B., Francois, P., Fritscher, K. and Schulz, U., EB-PVD processing of pyrochlore-structured $La_2Zr_2O_7$-based TBCs. *Surf. Coat. Technol.*, 2004, **182**, 175–183.
6. Ma, W., Gong, S. K., Xu, H. B. and Cao, X. Q., The thermal cycling behavior of lanthanum–cerium oxide thermal barrier coating prepared by EB-PVD. *Surf. Coat. Technol.*, 2006, **200**, 5113–5118.
7. Thornton, J. and Majumdar, Ceria precipitation and phase stability in zirconia based thermal barrier coatings. In *Proceedings of the International Thermal Spray Conference 95 (Kobe, Japan, May 1995), Thermal Spraying—Current Status and Future Trends*, ed. A. Ohmori. ASM Thermal Spray Society, Osaka, Japan, 1995, pp. 1075–1080.
8. Vassen, R., Tietz, F., Kerkhoff, G. and Stöver, D., New materials for advanced thermal barrier coatings. In *Proceedings of the 6th Liége Conference on "Materials for Advanced Power Engineering" (Universite de Liége, Belgium, November 1998)*, ed. J. Lecomte-Beckers, F. Schuber and P. J. Ennis. ASM Thermal Spray Society, Liége, Belgium, 1998, pp. 1627–1635.
9. Cao, X. Q., Vassen, R. and Stöver, D., Ceramic materials for thermal barrier coatings. *J. Eur. Ceram. Soc.*, 2004, **24**, 1–10.
10. Cemuschi, F., Bianchi, P., Leoni, M. and Scardi, P., Thermal diffusivity/microstructure relationship in Y–PSZ thermal barrier coatings. *J. Therm. Spray. Technol.*, 1999, **8**(1), 102–109.
11. Cao, X. Q., Vassen, R., Jungen, W., Schwartz, S., Tietz, F. and Stöve, D., Thermal stability of lanthanum zirconate plasma-sprayed coating. *J. Am. Ceram. Soc.*, 2001, **84**(9), 2086–2090.
12. Maloney, M. J., Thermal barrier coating systems and materials. European Patent No. EP 0848077 Al, 1998.
13. Vassen, R., Cao, X. Q., Tietz, F., Kerkhoff, G. and Stöver, D., $La_2Zr_2O_7$—a new candidate for thermal barrier coatings. In *Proceedings of the United Thermal Spray Conference 99 (Düsseldorf, Germany, March 1999)*, ed. E. Lugscheider and P. A. Kammer. ASM Thermal Spray Society, Düsseldorf, Germany, 1999, pp. 830–834.
14. Vassen, R., Cao, X. Q., Tietz, F., Basu, D. and Stöver, D., Zirconates as new materials for thermal barrier coatings. *J. Am. Ceram. Soc.*, 2000, **83**(8.), 2023–2028.
15. Bobzin, K., Lugscheider, E. and Bagcivan, N., Thermal cycling behavior of 8YSZ and LZ as graded and bilayer EB-PVD TBC. *High Temp. Mater. Processes*, 2006, **10**, 103–108.
16. Cao, X. Q., Vassen, R., Tietz, F. and Stöver, D., New double-ceramic-layer thermal barrier coatings based on zirconia–rare earth composite oxides. *J. Eur. Ceram. Soc.*, 2006, **26**, 247–252.
17. Zhou, H. M., Yi, D. Q., Yu, Z. M. and Xiao, L. R., Preparation and thermophysical properties of CeO_2 doped $La_2Zr_2O_7$ ceramic for thermal barrier coatings. *J. Alloys Compd.*, 2006, **438**, 217–222.
18. Cao, X. Q., Li, J. Y., Zhong, X. H., Zhang, J. F., Zhang, Y. F., Vassen, R. *et al.*, $La_2(Zr_{0.7}Ce_{0.3})_2O_7$—A new oxide ceramic material with high sintering-resistance. *Mater. Lett.*, 2008, **62**, 2667–2669.
19. Leushake, U., Krell, T., Schulz, U., Peters, M., Kaysser, W. A. and Rabin, B. H., Microstructure and phase stability of EB-PVD alumina and alumina/zirconia for thermal barrier coating applications. *Surf. Coat. Technol.*, 1997, **94/95**, 131–136.

20. Wortman, D. J., Nagaraj, B. A. and Duderstadt, E. C., Thermal barrier coatings for gas turbine use. *Mater. Sci. Eng. A*, 1989, **121**, 433–440.
21. Lugscheider, E., Barimani, C., Wolff, C., Guerreiro, S. and Doepper, G., Comparison of the structure of PVD—thin films deposited with different deposition energies. *Surf. Coat. Technol.*, 1996, **86/87**, 177–183.
22. Schulz, U., Saruhan, B., Fritscher, K. and Leyens, C., Review on advanced EB-PVD ceramic topcoats for TBC applications. *Int. J. Ceram. Technol.*, 2004, **1**(4), 302–315.
23. Pannetier, J., Energie electrostatique des reseaux pyrochlore. *J. Phys. Chem. Solids*, 1973, **34**, 583–587.
24. Schulz, U., Rätzer-Scheibe, H. J., Saruhan, B. and Renteria, A. F., Thermal conductivity issues of EB-PVD thermal barrier coatings. *Mat.-Wiss. Werkstofftech.*, 2007, **38**(9), 659–666.
25. Samsonov, G. V., *The Oxide Handbook* (*2nd ed.*). IFI/Plenum, New York, 1982.
26. Schulz, U. and Schmücker, M., Microstructure of ZrO_2 thermal barrier coatings applied by EB-PVD. *Mater. Sci. Eng. A*, 2000, **276**, 1–8.
27. Schulz, U., Terry, S. G. and Levi, C. G., Microstructure and texture of EB-PVD TBCs grown under different rotation modes. *Mater. Sci. Eng. A*, 2003, **360**, 319–329.
28. Bi, X. F., Xu, H. B. and Gong, S. K., Investigation of the failure mechanism of thermal barrier coatings prepared by electron beam physical vapor deposition. *Surf. Coat. Technol.*, 2000, **130**, 122–127.
29. Bansal, N. P. and Zhu, D. M., Thermal properties of oxides with magnetoplumbite structure for advanced thermal barrier coatings. *Surf. Coat. Technol.*, 2008, **202**, 2698–2703.
30. Miller, R. A., Current status of thermal barrier coatings—an overview. *Surf. Coat. Technol.*, 1987, **30**, 1–11.
31. Ma, W., Gong, S. K., Li, H. F. and Xu, H. B., Novel thermal barrier coatings based on $La_2Ce_2O_7$/8YSZ double-ceramic-layer systems deposited by electron beam physical vapor deposition. *Surf. Coat. Technol.*, 2008, **202**, 2704–2708.
32. Wang, X., Helmersson, U., Birch, J. and Ni, W., High resolution X-ray diffraction mapping studies on the domain structure of $LaAlO_3$ single crystal substrates and its influence on $SrTiO_3$ film growth. *J. Cryst. Growth*, 1997, **171**(3/4), 401–408.